

Atomistic Simulation of NO Dioxygenation in Group I Truncated Hemoglobin

Sabyashachi Mishra and Markus Meuwly*

Department of Chemistry, University of Basel, Basel, Switzerland

Received September 22, 2009; E-mail: m.meuwly@unibas.ch

Abstract: NO dioxygenation, i.e., the oxidation of nitric oxide to nitrate by oxygen-bound truncated hemoglobin (trHbN) is studied using reactive molecular dynamics simulations. This reaction is an important step in a sequence of events in the overall NO detoxification reaction involving trHbN. The simulations (≈ 160 ns in total) reveal that the reaction favors a pathway including (i) NO binding to oxy-trHbN, followed by (ii) rearrangement of peroxynitrite-trHbN to nitrate-trHbN, and finally (iii) nitrate dissociation from nitrate-trHbN. Overall, the reactions occur within tens of picoseconds and the crossing seam of the reactant and product are found to be broad. The more conventional pathway, where the peroxynitrite-trHbN complex undergoes peroxide cleavage to form free NO_2 and oxo-ferryl trHbN, is found to be too slow due to a considerable barrier involved in peroxide bond dissociation. The energetics of this step is consistent with earlier electronic structure calculations and make this pathway less likely. The role of Tyr33 and Gln58 in the NO dioxygenation has been investigated by studying the reaction in mutants of trHbN. The mutation study suggests that residues Tyr33 and Gln58 preorient the reactive ligands through a highly dynamical H-bonding network which facilitates the reaction. In particular, the Y33A mutation leads to a significant retardation in NO dioxygenation, in agreement with experiments which reveal a strong influence of the protein environment on the reaction rate.

Introduction

Heme proteins are well-known for their role in ligand transport.¹ With the recent discovery of heme proteins in the lower strata of the animal and plant kingdoms,^{2,3} these proteins have been established to be implicated in a range of functional roles including neurotransmission, inhibition of mitochondrial respiration, oxidative phosphorylation, catalytic peroxidation, and NO scavenging.^{4–7} NO scavenging, where the toxic NO is converted to harmless nitrate, has wide-ranging physiological significance.⁸ This reaction was first reported in myoglobin (Mb) by Doyle et al.,⁹ which has since been extensively studied by various experimental and computational methods. Recent NMR studies of the reaction provide concrete evidence of NO dioxygenation in myoglobin.¹⁰ From stopped-flow spectroscopy, the second-order rate constants for the reaction between NO and oxy-myoglobin and oxy-hemoglobin, at neutral pH, are

determined to be 4.36×10^7 and $8.9 \times 10^7 \text{ M}^{-1} \text{ s}^{-1}$, respectively.^{11,12} However, the details and sequence of events that constitute the reaction mechanism and nature of the intermediates remain elusive.¹³

With the employment of stopped flow kinetic measurements, Bourassa et al. proposed a reaction pathway for NO oxidation in Mb where the peroxynitrite (Fe(III)OONO) intermediate undergoes O–O homolysis to form free nitrite radicals (NO_2).¹⁴ In this model, the free nitrite radical then binds to the oxo-ferryl (Fe(IV)=O) group to form the nitrate complex (Fe(III)ONO_2), which ultimately leads to free nitrate. This reaction mechanism proposes heme-bound peroxynitrite, oxo-ferryl with free NO_2 , and heme-bound nitrate intermediates for the NO oxidation reaction.¹⁴ A similar pathway is also observed when peroxynitrite is reacted with metmyoglobin.¹⁵ On the other hand, Herold et al. have provided evidence for a Fe(III)OONO (high-spin) intermediate in both oxy-Mb and oxy-Hb by rapid-scan ultraviolet–visible (UV–vis) spectroscopy,^{12,16} which was later corroborated via electron paramagnetic resonance (EPR) spectroscopy.¹⁷ This intermediate is however only observed

- (1) Wittenberg, J. B. *Physiol. Rev.* **1970**, *50*, 559–636.
- (2) Kundu, S.; Trent, J. T.; Hargrove, M. S. *Trends Plant Sci.* **2003**, *8*, 387–393.
- (3) Garrocho-Villegas, V.; Gopalasubramaniam, S. K.; Arredondo-Peter, R. *Gene* **2007**, *398*, 78–85.
- (4) Wittenberg, J. B.; Wittenberg, B. A. *J. Exp. Biol.* **2003**, *206*, 2011–2020.
- (5) Merx, M. W.; Goedecke, A.; Floegel, U.; Schrader, J. *FASEB J.* **2005**, *19*, 1015–1017.
- (6) Garry, D. J.; Meeson, A.; Yan, Z.; Williams, R. S. *Cell. Mol. Life Sci.* **2000**, *57*, 896–898.
- (7) Marinis, E.; Casella, L.; Ciaccio, C.; Coletta, M.; Visca, P.; Ascenzi, P. *IUBMB Life* **2009**, *61*, 62–73.
- (8) Hausladen, A.; Gow, A.; Stamler, J. S. *Proc. Natl. Acad. Sci. U.S.A.* **2001**, *98*, 10108–10112.
- (9) Doyle, M. P.; Hoekstra, J. W. *J. Inorg. Biochem.* **1981**, *14*, 351–358.
- (10) Floegel, U.; Merx, M. W.; Goedecke, A.; Decking, U. K. M.; Schrader, J. *Proc. Natl. Acad. Sci. U.S.A.* **2001**, *98*, 735–740.

- (11) Eich, R. F.; Li, T.; Lemon, D. D.; Doherty, D. H.; Curry, S. R.; Aitken, J. F.; Mathews, A. J.; Johnson, K. A.; Smith, R. D.; Phillips, G. N., Jr.; Olson, J. S. *Biochemistry* **1996**, *35*, 6976–6983.
- (12) Herold, S.; Exner, M.; Nauser, T. *Biochemistry* **2001**, *40*, 3385–3395.
- (13) Gardner, P. R.; Gardner, A. M.; Brashear, W. T.; Suzuki, T.; Hvitved, A. N.; Setchell, K. D.; Olson, J. S. *J. Inorg. Biochem.* **2006**, *100*, 542–550.
- (14) Bourassa, J. L.; Ives, E. L.; Marqueling, A. L.; Shimanovich, R.; Groves, J. T. *J. Am. Chem. Soc.* **2001**, *123*, 5142–5143.
- (15) Su, J.; Groves, T. *J. Am. Chem. Soc.* **2009**, *131*, 12979–12988.
- (16) Herold, S. *FEBS Lett.* **1999**, *443*, 81–84.
- (17) Olson, J. S.; Foley, E. W.; Rogge, C.; Tsai, A.-L.; Doyle, M. P.; Lemon, D. D. *Free Radical Biol. Med.* **2004**, *36*, 685–697.

under alkaline conditions (pH = 9.5).^{12,17} At neutral pH, the reaction proceeds without any observed intermediates,¹² suggesting a rapid rearrangement of the Fe(III)OONO intermediate to nitrate. The kinetics of the intermediate in NO dioxygenation is found to be strongly influenced by pH.¹² The pH dependence of the intermediate has been investigated with density functional theory (DFT) calculations on models that mimic the active site of the protein at different pH.¹⁸ However, the computations did not provide an unambiguous explanation of the observed pH dependence of the decay rate of the intermediate. Additionally, in the experiments of Herold et al., no detectable OONO⁻ or NO₂⁻ are released,^{12,16} which is at variance with the pathway proposed by Groves and co-workers.^{14,15} Herold et al. observed quantitative nitrate formation and concluded that the peroxynitrite coordinated to heme-Fe rapidly undergoes a rearrangement to nitrate without nitrating the globin residues.¹² Their analysis is, however, inconclusive so as to decide if the rearrangement is concerted or not, since the lack of detection of oxo-ferryl species (obtained from O–O homolysis of the peroxynitrite species) may either indicate that the intermediate is not formed at all or it might react too fast to accumulate for experimental detection.

In a reaction of NO₂ with oxo-ferryl myoglobin, a rate of $1.2 \times 10^7 \text{ M}^{-1} \text{ s}^{-1}$ for the oxidation of NO₂ to nitrate via the Fe(III)ONO₂ intermediate was found.¹⁹ The assignment of the intermediate was based on thermo-kinetic arguments, and it was suggested that the intermediates observed in both, the Fe(IV)=O + NO₂ reaction (ref 19) and the Fe(II)–O₂ + NO reaction (ref 12) are the same, i.e., Fe(III)ONO₂, which is in contrast to the peroxynitrite intermediate reported in oxy-myoglobin¹² (see previous paragraph). The Fe(III)ONO₂ intermediate has a similar decay constant ($190 \pm 20 \text{ s}^{-1}$) as the Fe(III)OONO intermediate ($205 \pm 5 \text{ s}^{-1}$) reported earlier.¹² It should be noted that the evidence for the peroxynitrite intermediate obtained from EPR spectroscopy in ref 17 cannot unambiguously distinguish between Fe(III)ONO₂ and Fe(III)OONO.²⁰ In a recent resonance Raman study, the intermediate in myoglobin has been assigned to the Fe(III)ONO₂ complex,²¹ although the temporal resolution of the experiment does not allow one to determine whether the peroxynitrite intermediate is formed during the reaction.²¹

DFT calculations for model heme systems have suggested that the reaction progresses via the peroxynitrite (Fe(III)OONO) intermediate which rapidly undergoes homolytic O–O bond fission, and the resulting NO₂ recombines with oxo-ferryl (Fe(IV)=O) species even faster.¹⁸ Each of the steps are found to have moderate to large (2–10 kcal/mol) activation barriers. From electronic structure calculations, it was concluded that the peroxynitrite intermediate is too short-lived to have been experimentally detected. It should be noted that the DFT calculation finds a low-spin peroxynitrite instead of a high-spin Fe(III)OONO as suggested from EPR experiments.¹⁷

In plant hemoglobin (leghemoglobin or Lb), even under alkaline conditions, no intermediate in the NO oxidation reaction was reported,²² whereas a reactive intermediate (Fe(III)OONO or Fe(III)ONO₂) was detected for the reaction in Hb and Mb at

alkaline pH.¹² The observation that the intermediate decays considerably faster in Lb than in Hb/Mb suggests that the protein environment is important for details of the reaction. A major difference between the structures of Hb/Mb and Lb is the presence of a wider and more flexible heme pocket in Lb.²³ The mechanistic details of NO dioxygenation is likely to be influenced by the distal site residues of the particular globin chain, and hence, intermediates found in one type of globin do not necessarily occur in other globins.

The role of flavohemoglobins (FHb, a group of hemoglobins found in bacteria and yeasts) in protecting against nitrosative stress is now well established.^{8,24,25} While under aerobic conditions, O₂ is the preferred ligand for binding to heme, it has been shown that under physiological NO/O₂ concentrations, FHbs bind NO at the heme iron and catalyze the reaction of heme-bound NO with O₂ to produce nitrate.⁸ The reaction where the heme-bound O₂ oxidizes free NO has the advantage of high reactivity of both, the free NO radical as well as the superoxide nature of heme-bound O₂. The reaction of bound NO and free O₂ in FHbs, on the other hand, is assisted by the presence of a flavoreductase domain together with Hb.²⁶ For human Hb, the reaction of heme-bound NO with free O₂ has been shown to proceed in three steps, where the first step involves the dissociation of NO radical from heme, which then binds to O₂, and finally the bound O₂ oxidizes free NO.^{27,28}

In truncated hemoglobin N (trHbN) of *Mycobacterium tuberculosis*, the rate for NO dioxygenation is faster compared to that in vertebrate Mbs and Hbs. It was suggested that this is due to a tunnel system in the protein matrix and ligand stabilizing residues in the heme active site.²⁹ Irrespective of the reaction mechanism, it is commonly agreed that the diffusion controlled migration of the ligand to the heme active site is the slowest process in NO detoxification and, hence, it is the rate determining step.^{11,30} The second order rate constant of NO reaction with oxy-trHbN is determined to be $7.5 \times 10^8 \text{ M}^{-1} \text{ s}^{-1}$, which is about an order of magnitude faster than in vertebrate Hb.²⁹ The in vitro kinetics for NO dioxygenation in oxy-trHbN is studied under aerobic conditions,²⁹ although in vivo trHbN operates at microaerobic conditions. Under such circumstances, which ligand binds to the heme is determined by the relative abundance of NO and O₂ as well as the ligand affinity of the protein. In group II truncated hemoglobin (trHbO) of *Mycobacterium tuberculosis*, the rate constant for NO binding to deoxygenated trHbO ($0.18 \mu\text{M}^{-1} \text{ s}^{-1}$ (80%) and $0.95 \mu\text{M}^{-1} \text{ s}^{-1}$ (20%)) is only marginally larger than the corresponding rate constant for O₂ binding ($0.11 \mu\text{M}^{-1} \text{ s}^{-1}$ (80%) and $0.85 \mu\text{M}^{-1} \text{ s}^{-1}$ (20%)).^{31,32} For trHbN of *Mycobacterium tuberculosis*,

- (18) Blomberg, L. M.; Blomberg, M. R. A.; Siegbahn, P. E. M. *J. Biol. Inorg. Chem.* **2004**, *9*, 923–935.
 (19) Goldstein, S.; Merenyi, G.; Samuni, A. *J. Am. Chem. Soc.* **2004**, *126*, 15694–15701.
 (20) Hvitved, A.; Foley, E.; Rogge, C.; Tsai, A.-L.; Olson, J. *Free Radical Biol. Med.* **2005**, *39*, S101–S101.
 (21) Yukl, E. T.; de Vries, S.; Moenne-Loccoz, P. *J. Am. Chem. Soc.* **2009**, *131*, 7234–7235.
 (22) Herold, S.; Puppo, A. *J. Biol. Inorg. Chem.* **2005**, *10*, 935–945.

- (23) Hargrove, M. S.; Barry, J. K.; Brucker, E. A.; Berry, M. B.; Phillips, G. N., Jr.; Olson, J. S.; Arredondo-Peter, R.; Dean, J. M.; Klucas, R. V.; Sarath, G. *J. Mol. Biol.* **2007**, *266*, 1032–1042.
 (24) Gardner, P. R.; Gardner, A. M.; Martin, L. A.; Salzman, A. L. *Proc. Natl. Acad. Sci. U.S.A.* **1998**, *95*, 10378–10383.
 (25) Hausladen, A.; Gow, A. J.; Stamler, J. S. *Proc. Natl. Acad. Sci. U.S.A.* **1998**, *95*, 14100–14105.
 (26) Ermler, U.; Siddiqui, R. A.; Cramm, R.; Friedrich, B. *EMBO J.* **1995**, *14*, 6067–6077.
 (27) Herold, S.; Rock, G. *Biochemistry* **2005**, *16*, 6223–6231.
 (28) Moller, J. K. S.; Skibsted, L. H. *Chem.—Eur. J.* **2004**, *10*, 2291–2300.
 (29) Ouellet, H.; Ouellet, Y.; Richard, C.; Labarre, M.; Wittenberg, B.; Wittenberg, J.; Guertin, M. *Proc. Natl. Acad. Sci. U.S.A.* **2002**, *99*, 5902–5907.
 (30) Angelo, M.; Hausladen, A.; Singel, D.; Stamler, J. S. *Methods Enzymol.* **2008**, *436*, 131–168.
 (31) Ouellet, H.; Juszczak, L.; Dantsker, D.; Samuni, U.; Ouellet, Y. H.; Savard, P.-Y.; Wittenberg, J. B.; Wittenberg, B. A.; Friedman, J. M.; Guertin, M. *Biochemistry* **2003**, *42*, 5764–5774.

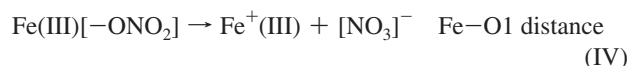
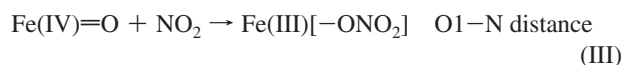
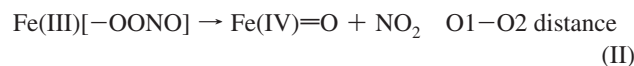
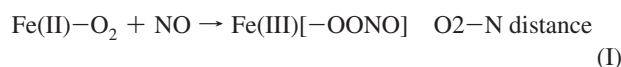
which is the protein investigated here, the corresponding rate constant was only determined for O₂ binding ($25 \mu\text{M}^{-1} \text{s}^{-1}$).^{32,33} In *Mycobacterium leprae*, the O₂-mediated oxidation of trHbO-NO occurs with a reaction mechanism in which the heme-bound NO is displaced by the O₂ ligand in the first step followed by the reaction of NO with the oxy-trHbO to give rise to nitrate.³⁴ Given this sequence of events and the typically higher affinity of Fe(II) toward NO than to O₂, it is likely that under physiological conditions NO dioxygenation of O₂-bound heme is one step, probably the last one, in a sequence of events in NO detoxification. As far as possible intermediates of NO dioxygenation are concerned, there has been no experimental kinetics studies for trHbN. For oxy-trHbN, where the reaction is 20 times faster at physiological conditions, no pH dependence of the NO dioxygenation is known,²⁹ contrary to oxy-Mb. Furthermore, unlike that of flavohemoglobins,⁸ no steady state turnover of NO or mass balance accounting of product has been reported so far for trHb.³⁰

Over the years, mixed quantum mechanics/molecular mechanics (QM/MM) has been used to study chemical reactions in biological systems. In QM/MM, the reacting atoms are described by quantum mechanics which are then embedded in the classical force field of the surrounding atoms.^{35–37} The computationally demanding QM part is the bottleneck of the method that dictates the accessible time scale of the simulations. Except for cases where the QM part is treated with semiempirical methods, the nuclear dynamics and conformational sampling are typically not included in such studies. This is also the case for the QM/MM work carried out so far on the reactions of interest in the present work (see below).^{38,39} An alternative approach to study chemical reactions in condensed phases is to use empirical force fields with provisions to form and break bonds. One such approach is empirical valence bond (EVB)⁴⁰ which has been extensively used to investigate catalytic reactions in biological systems. An alternative to EVB is adiabatic reactive molecular dynamics (ARMD) which has been recently proposed.^{41–43} In ARMD, the reactant and product are treated with individually parametrized force fields which differ in a small number of terms. The algorithm employs an energy criterion to decide when a crossing should occur. After a crossing is detected, the two states are mixed over a short period of time, and the simulation continues on the second surface.^{42,43} Such an approach allows one to efficiently treat bond breaking and bond formation reactions in the framework of classical MD

simulations. With the use of ARMD, the nonexponential re-binding of NO in myoglobin⁴² and the conformational equilibrium in neuroglobin⁴³ have been previously studied and provide quantitative and novel insight into mechanistic aspects of the reactions.

The fact that detailed experimental studies on NO dioxygenation in trHbN is rather scarce and the corresponding studies in Mb and Hb provide conflicting and inconclusive views on the mechanism of the reaction^{12,14,19,21} provides a strong motivation to use state-of-the-art computational techniques to investigate the energetics and dynamics of this interesting and challenging reactive system. In the present work, we have studied the mechanistic details of the oxidation of nitric oxide to nitrate by oxy-trHbN which recently has received considerable experimental and computational attention.^{18,29,38} The reaction between oxy-trHbN and NO is one of the steps in a sequence of events during overall NO detoxification involving trHbN under physiological conditions.

The NO dioxygenation in trHbN is about an order of magnitude faster than in human Hb, which makes it an ideal target for atomistic simulations. For this, ARMD is used together with force fields for the reactive intermediates determined from ab initio electronic structure calculations. The entire reaction is divided into the following four steps:



The right-hand side column of the above reaction steps indicates the bond broken/formed in the reaction step. In step I, the oxy-trHbN reacts with free NO to form a peroxyxynitrite intermediate complex which then undergoes homolytic fission. Step II involves production of the oxo-ferryl species and the free NO₂ radical. The free NO₂ radical then attacks the oxo-ferryl species to form the heme-bound nitrate complex (step III). Finally, the dissociation of the Fe–O bond results in free NO₃[−] and pentacoordinated heme (step IV). We have studied each of the above reaction steps by analyzing the structural and energetic requirement for the reaction, by characterizing the reaction seam, and by estimating the kinetics of these steps. Furthermore, we have explored the role of the protein in the NO dioxygenation by studying the above steps in different trHbN mutants. Finally, an alternative pathway which involves a peroxyxynitrite to nitrate rearrangement is investigated because a number of key intermediates postulated by steps I–IV were not observed experimentally.

Computational Methods

Molecular Dynamics Simulations. The initial structure of the protein is monomer A of the X-ray structure, protein data bank entry 1IDR. The protein contains 131 amino acid residues, a prosthetic heme group to which O₂ is bound, and an NO ligand. All MD simulations are carried out with the CHARMM22 force field⁴⁴ and the CHARMM program.⁴⁵ Nonbonded interactions are truncated at a distance of 14 Å by using a shift function for the electrostatic terms and a switch algorithm for the van der Waals

- (32) Milani, M.; Pesce, A.; Nardini, M.; Ouellet, H.; Ouellet, Y.; Dewilde, S.; Bocedi, A.; Ascenzi, P.; Guertin, M.; Moens, L.; Friedman, J. M.; Wittenberg, J. B.; Bolognesi, M. *J. Inorg. Biochem.* **2005**, *99*, 97–109.
- (33) Couture, A.; Yeh, S.-R.; Wittenberg, B. A.; Wittenberg, J. B.; Ouellet, Y.; Rousseau, D. L.; Guertin, M. *Proc. Natl. Acad. Sci. U.S.A.* **1999**, *96*, 11223–11228.
- (34) Ascenzi, P.; Bolognesi, M.; Visca, P. *Biochem. Biophys. Res. Commun.* **2007**, *357*, 809–814.
- (35) Warshel, A.; Levitt, M. *J. Mol. Biol.* **1976**, *103*, 227–249.
- (36) Singh, U. C.; Kollman, P. A. *J. Comput. Chem.* **1986**, *7*, 718–730.
- (37) Field, M. J.; Bash, P. A.; Karplus, M. *J. Comput. Chem.* **1990**, *11*, 700–733.
- (38) Crespo, A.; Martí, M. A.; Kalko, S. G.; Morreale, A.; Orozco, M.; Gelpi, J. L.; Luque, F. J.; Estrin, D. A. *J. Am. Chem. Soc.* **2005**, *127*, 4433–4444.
- (39) Martí, M. A.; Bidon-Chanal, A.; Crespo, A.; Yeh, S.-R.; Guallar, V.; Luque, F. J.; Estrin, D. A. *J. Am. Chem. Soc.* **2008**, *130*, 1688–1693.
- (40) Warshel, A.; Weiss, R. M. *J. Am. Chem. Soc.* **1980**, *102*, 6218–6226.
- (41) Meuwly, M.; Becker, O. M.; Stone, R.; Karplus, M. *Biophys. Chem.* **2002**, *98*, 183–207.
- (42) Nutt, D.; Meuwly, M. *Biophys. J.* **2006**, *90*, 1191–1201.
- (43) Danielsson, J.; Meuwly, M. *J. Chem. Theory Comput.* **2008**, *4*, 1083–1093.

(vdW) terms.⁴⁶ All bonds involving hydrogen atoms are kept fixed by using SHAKE.⁴⁷ Initially, missing H atoms are added and histidine residues are treated as δ -protonated. The heme group is covalently bound to the N_e of residue His81, and the dioxygen molecule is ligated to the Fe(II) atom of the heme group, while the NO ligand is initially unbound. Since the aim of the simulations is to study the redox reaction occurring in the active site surrounding the heme group, the stochastic boundary method was used to increase computational efficiency.⁴⁸ The heme active site was solvated by a water sphere of radius 25 Å, and the reaction region, where Newtonian dynamics is used, had a radius of 20 Å. Water molecules that overlap protein atoms are removed and a short minimization was done. Then Langevin dynamics was performed for heating and equilibration during 500 ps (at 300 K). The water molecules are represented with the modified TIP3P potential.⁴⁹ The entire solvated system contains 6867 atoms.

Reactions I–IV are studied by employing the recently developed ARMD algorithm.^{42,43} In this method, the potential energy surfaces of the reactants V_R and products V_P are described with empirical force fields that correctly describe geometric, energetic, and other physical properties of the reactant and product states. Since V_R and V_P are parametrized individually, they differ by a constant Δ which corresponds to the asymptotic energy difference between the two states^{40,42,43} and which is the only free parameter in ARMD. In other words, Δ ensures that V_R and V_P share a common zero of energy. The system is propagated on the lower of the two surfaces by solving Newton's equations of motion and the energy difference $\Delta E = V_R - V_P$ is monitored. A surface crossing occurs whenever ΔE changes sign, and the system is promoted from one state to the next by mixing the two potential energy surfaces (PESs) over a short time window (typically a few femtoseconds).^{42,43}

The asymptotic energy difference Δ is determined as follows. If sufficient experimental data is available (e.g., interconversion rates),⁴³ Δ is chosen to reproduce such quantities. In the absence of suitable reference quantities, an initial Δ_0 is used from ab initio calculations. In a next step, the sensitivity of the computed observables (here reaction rates and the reaction seam) is assessed through variation of Δ around Δ_0 . This procedure is reminiscent of ab initio parametrizations of EVB^{40,50} or of approximate valence bond (AVB)⁵¹ although the parametrization of an off-diagonal matrix element as a function of a configurational coordinate is not necessary in ARMD, since the only progression coordinate in ARMD is time. Δ is expected to be influenced by structural changes and the solvent environment which differentially stabilizes/destabilizes the reactants or products. Therefore, microscopically Δ should be viewed as an averaged quantity. In comparing EVB with ARMD it is interesting to note that in the former a similar quantity arises as the gas-phase formation energy of X^-Y^+ from XY at infinite separation.⁴⁰ When a bond-breaking/bond-formation reaction is studied in a protein environment with ARMD, Δ cannot be calculated from electronic structure calculations because its value depends on the instantaneous configuration of the system and therefore it is only meaningful to view Δ as a conformationally averaged quantity. To sample configurational space, six snapshots of the reactants in each of the reaction steps (reactions I–IV) were considered and multiple ARMD trajectories from each of the initial snapshots were initiated. This is done for a range of Δ values for each of the reaction steps studied in this work.

Ab Initio Determination of Force Field. The necessary force fields for the different states in reactions I–IV were derived from electronic structure calculations at the DFT/B3LYP level with the 6-31G** basis set that were carried out with Gaussian.⁵² The model system contains the porphyrin ring, Fe atom, and an imidazole ring representing the proximal histidine and the O₂ and NO ligands. The geometries of all five states in reactions I–IV were optimized in each of their lowest three spin multiplicities (doublet, quartet, and sextet), and the most stable spin multiplet is considered for further investigation. All calculations were carried out with the polarized continuum model (PCM), with $\epsilon = 4$, which corresponds to a dielectric constant of protein and water medium surrounding the protein.⁵³ The present ab initio calculations are validated by comparing them with previous work^{18,38} (see also the Supporting Information). In particular, it was found that bound OONO is more stable than free NO by 17.6 and 19.3 kcal/mol, in the gas and solvent phases, respectively, which compares well with values obtained previously, which are 13 and 15 kcal/mol, respectively.^{18,38} The remaining energetics are very similar to the results from Blomberg et al. but they differ substantially from those by Crespo et al., which employs, unlike the present work or the work of Blomberg et al., a pseudopotential-based DFT method.^{18,38} Further details are given in the Supporting Information. Mulliken charges were calculated at the optimized geometries. Compared to the charges used in the CHARMM force field, Mulliken charges are often found to be too large. Therefore, they were rescaled in the following way:⁵⁴ First, the charges of the Fe and N-porphyrin atoms were scaled to reproduce CHARMM charges for the heme system (Table S1 in the Supporting Information), which leads to a net charge of the heme group that differs from its usual value of -2 . The residual charge is then redistributed over the C atoms of the porphyrin ring of the heme. An overview of all charges is given in Table S2 in the Supporting Information. As can be seen, the residual charges are often negligibly small.

Harmonic force constants for internal coordinates were determined from five energies calculated along the respective coordinate around its equilibrium value. For bond lengths, the grid spacing is 0.01 Å whereas for bond angles and dihedrals it is 5°. The harmonic force constants are determined from the second derivative of the energy using the five-point rule⁵⁵

$$f''(x) \approx \frac{-f(x-2h) + 16f(x-h) - 30f(x) + 16f(x+h) - f(x+2h)}{12h^2} \quad (1)$$

where h is the grid spacing. Since the bonds undergoing breaking and formation in steps I–IV exhibit large fluctuations, the potential energy curves are calculated over a wide range for bond distances between 1 and 4 Å and the resulting energy profiles are fit to Morse functions

$$V_M = D_e [1 - \exp(-\beta(r - r_0))]^2 \quad (2)$$

where D_e is the bond dissociation energy, β is the width of the potential, and r_0 is the equilibrium bond distance.

To validate the interaction potentials, total energies for snapshots corresponding to the reactant, product, and the crossing points obtained from five arbitrarily chosen ARMD trajectories for step I were determined from DFT/6-31G** single point calculations, see Figure 9 for energy differences between the reactant, product, and transition state (TS) structures. The system which was used for these

(44) MacKerell, A. D., Jr.; et al. *J. Phys. Chem. B* **1998**, *102*, 3586–3616.

(45) Brooks, B.; Bruccoleri, R.; Olafson, B.; States, D.; Swaminathan, S.; Karplus, M. *J. Comput. Chem.* **1983**, *4*, 18–217.

(46) Steinbach, P. J.; Brooks, B. R. *J. Comput. Chem.* **1994**, *15*, 667–683.

(47) van Gunsteren, W.; Berendsen, H. *Mol. Phys.* **1977**, *34*, 1311–1327.

(48) Brooks, B.; Karplus, M. *J. Chem. Phys.* **1983**, *79*, 6312–6325.

(49) Jorgensen, W. L.; Chandrasekhar, J.; Madura, J. D.; Impey, R. W.; Klein, M. L. *J. Chem. Phys.* **1983**, *79*, 926–935.

(50) Chang, Y.-T.; Miller, W. H. *J. Phys. Chem.* **1990**, *94*, 5884–5888.

(51) Grochowski, P.; Lesyng, B.; Bala, P.; McCammon, J. A. *Int. J. Quantum Chem.* **1996**, *60*, 1143–1164.

(52) Frisch, M. J.; et al. *Gaussian 03*, revision C.02; Gaussian, Inc.: Wallingford, CT, 2004.

(53) Blomberg, M. R. A.; Siegbahn, P. E. M.; Babcock, G. T. *J. Am. Chem. Soc.* **1998**, *120*, 8812–8824.

(54) Nutt, D.; Meuwly, M. *ChemPhysChem* **2004**, *5*, 1710–1718.

(55) Abramowitz, M.; Stegun, I. A. *Handbook of Mathematical Functions with Formulas, Graphs, and Mathematical Tables*; Dover: New York, 1970.

Table 1. Differential Force Fields between Two Given Atoms in ARMD Simulation for Reaction Steps I–IV^a

atom1–atom2	trHbN–O ₂ + NO	trHbN–O ₂ NO
O2–N	nonbonded	Morse potential
O1–N	nonbonded	bond angle via O2
O2–O	nonbonded	bond angle via N
O1–O	nonbonded	dihedral via O2–N
Fe–N	nonbonded	dihedral via O1–O2

atom1–atom2	trHbN–O ₂ NO	trHbN=O + NO ₂
O1–O2	Morse potential	Nonbonded
O1–N	bond angle via O2	Nonbonded
Fe–O2	bond angle via O1	Nonbonded
O1–O	dihedral via O2–N	Nonbonded
Fe–N	dihedral via O1–O2	Nonbonded
O2–N ϵ of H81	dihedral via O1–Fe	Nonbonded

atom1–atom2	trHbN=O + NO ₂	trHbN–ONO ₂
O1–N	nonbonded	Morse potential
Fe–N	nonbonded	bond angle via O1
Fe–O2/O	nonbonded	dihedral via O1–N
O1–O2/O	nonbonded	bond angle via N
N–N ϵ of H81	nonbonded	dihedral via O1–Fe

atom1–atom2	trHbN–ONO ₂	trHbN + NO ₃ [–]
Fe–O1	Morse potential	nonbonded
Np–O1	angle via Fe	nonbonded
Fe–N	bond angle via O1	nonbonded
Fe–O2/O	dihedral via O1–N	nonbonded
N–N ϵ ₂ of H81	dihedral via O1–Fe	nonbonded

^a Nonbonded interactions include electrostatic and van der Waals terms. H81 is the proximal histidine attached to Fe atom of heme.

calculations (see Figure S1 in the Supporting Information) is identical to the one for which the parametrization was carried out. It is found that the energetic ordering between reactant, product, and TS from both types of calculations (compare Figures S2 in the Supporting Information and Figure 9) agree and therefore we expect that the force field gives realistic energetics for investigating the reactions. It can also be seen that conformational sampling influences and modulates the relative energies of transition state and product relative to the reactant. Further validations are provided in the Discussion and Conclusions.

Results

Dynamics of NO Dioxygenation in trHbN. Step I: NO Binding to oxy-trHbN. In step I, the free NO ligand attacks the heme-bound O₂ to form a bound peroxy-nitrite complex. In the product, a bond between the O2 atom of O₂ and the N atom of NO is formed which also gives rise to additional angles (Table 1). In a first approximation, $\Delta_0 = 25.6$ kcal/mol, which corresponds to the dissociation energy of the O2–N Morse potential. As the potential energy surfaces describing the two states are multidimensional, Δ will differ somewhat from Δ_0 and the grid for Δ included $\Delta = 60, 30, 26, 15,$ and 5 kcal/mol. From six snapshots of oxy-trHbN with free NO (see Figure 1 for the relative positions of ligands and heme plane), multiple 50 ps trajectories were started with different initial velocities.

The geometric characterization of the crossing seam is presented in parts A and B of Figure 2. While Fe–O1, O1–O2, and N–O distances during the crossing events are more or less centered around their respective equilibrium values for all values of Δ , the rebinding takes place over a broad range of O2–N distances, see Figure 2A. For $\Delta = 60, 30,$ and 26 kcal/mol, the crossing seam along the O2–N coordinate ranges from 2.7 to

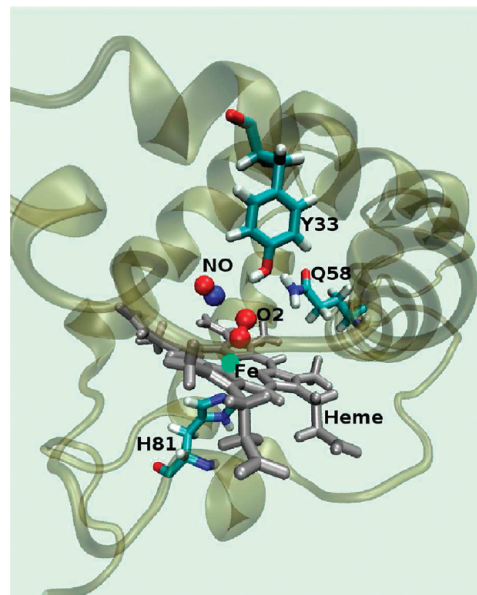


Figure 1. Ribbon representation of trHbN showing the heme plane, the reactive ligands (O₂ and NO), and the active site residues Y33 and Q58. The H81 residue is shown in the proximal side of the heme plane. The Fe atom of the heme is shown as a green sphere.

5.0 Å and centers around 3.2 Å. Concomitantly, a wide range of angles Fe–O1–O2, O1–O2–N, and O2–N–O (Figure 2A) are found at the crossing geometries. The distribution of dihedrals in Figure 2A suggests that both cis and trans OONO are possible during crossing whereas an exclusive trans geometry for the Fe–O1–O2–N dihedral is favored. Figure 2B shows a two-dimensional plot of O2–N distance versus O1–O2–N angle at the crossings for $\Delta = 60, 30, 26,$ and 15 kcal/mol. It is evident that the crossing geometries only weakly depend on the precise value of Δ and that the crossing seam is rather broad.

Figure 2C analyzes the time dependence of crossing events where the survival probability $p(t)$ of free NO is shown as a function of simulation time (t) for $\Delta = 60, 30, 26,$ and 15 kcal/mol. $p(t)$ can be fit to an exponential function, $p(t) = \exp(-t/\tau)$, to describe the underlying kinetics, where τ is the associated time constant. Table 2 summarizes the fitted time constants. For $\Delta = 60$ kcal/mol, the reaction is essentially monophasic with $\tau = 1.5$ ps and increases to 11 and 16 ps for $\Delta = 30$ and 26 kcal/mol, respectively. The fastest crossings occur within 70–100 fs. This suggests that an exclusive geminate recombination between bound O₂ and free NO occurs. For $\Delta = 15$ kcal/mol, only 25% of the trajectories showed rebinding, which leads to a longer time constant of about 200 ps.

It is also of interest to analyze the H-bonding network (between Tyr33, Gln58, O₂, and NO) during the crossing events. Figure 2D reports the probability distribution of the distance between some of the H-bonding partners. During most of the crossing events, H-bonding between the amide group of Gln58 and the phenol group of Tyr33 is observed (upper panel of Figure 2D) where TyrO acts as a H-bond acceptor of amide N of Gln58 and Tyr33 remains close to the reacting ligands. While for many crossings Tyr33 is a H-bond donor to the O2 atom of O₂, in some of the cases it participates in H-bonding with the O atom of NO. Nevertheless, crossings also take place even when Tyr33 is at a non-hydrogen-bonding distance from the ligand, see Figure 2D. A H-bond between Tyr33 and NO or O₂ suggests that the amino acid influences the movement of the ligands (NO/O₂), thus making it available for reaction I. Thus,

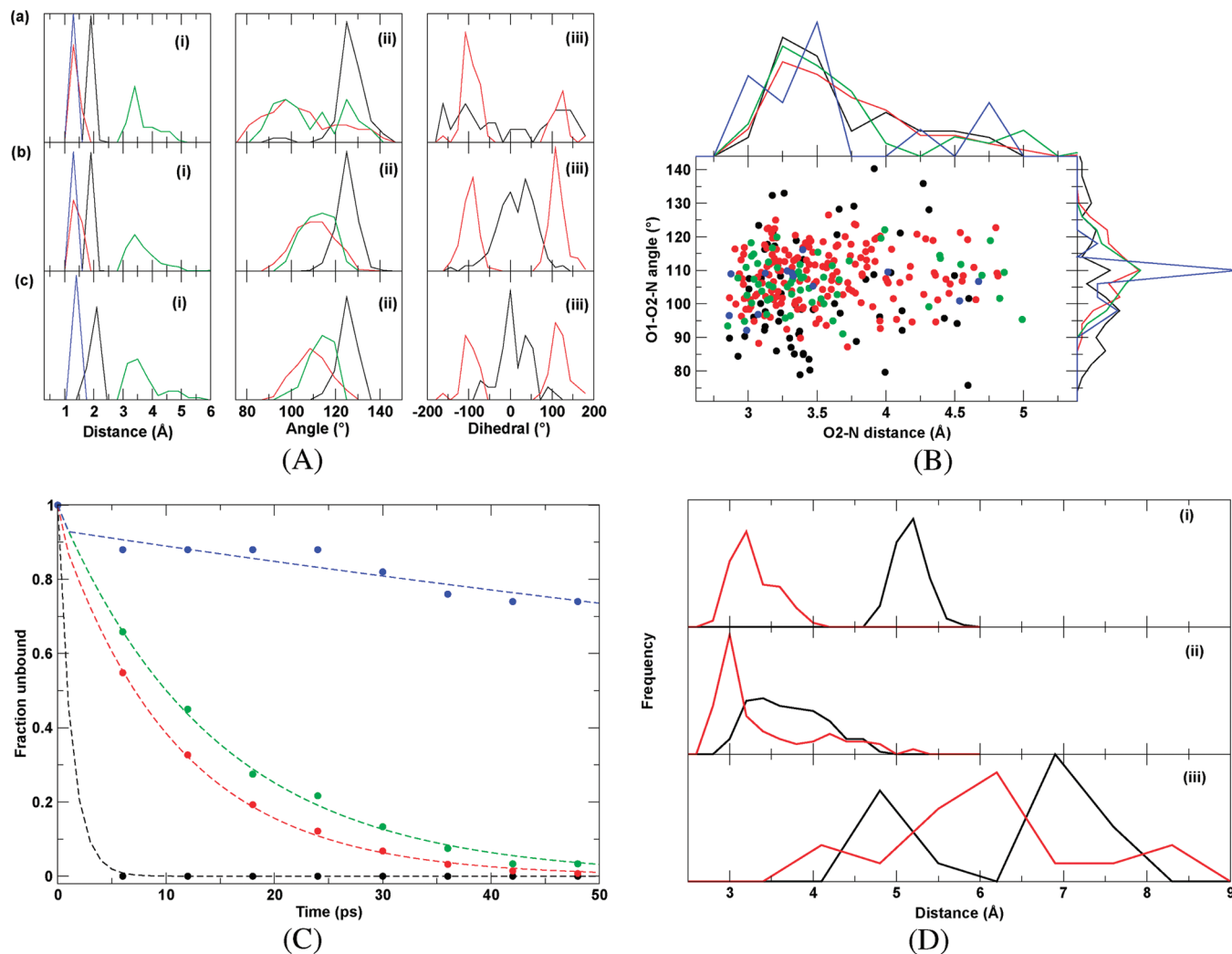


Figure 2. (A) Probability distribution of (i) bond distances [Fe–O (black), O1–O2 (red), O2–N (green), and N–O (blue)]; (ii) bond angles [Fe–O1–O2 (black), O1–O2–N (red), and O2–N–O (green)]; and (iii) dihedrals [O1–O2–N–O (black), Fe–O1–O2–N (red)] at the crossing points for NO rebinding oxy-trHbN with $\Delta =$ (a) 30, (b) 26, and (c) 15 kcal/mol, respectively. (B) Two-dimensional plot showing the correlated distribution of crossing points along the O2–N distance and O1–O2–N angle. The circles in black, red, green, and blue represent the crossings obtained with $\Delta = 60, 30, 26,$ and 15 kcal/mol, respectively. The corresponding one-dimensional distribution along O2–N and O1–O2–N coordinates are also shown. (C) Time distribution of fraction of trajectories without crossing for $\Delta = 60, 30,$ and 26 kcal/mol, shown in black, red, and green, respectively. (D) Probability distribution of the H-bonding network between Q58, Y33, bound O₂, and NO during the rebinding of NO. The distribution is shown for distances between (i) O atom of Y33 (O_{Y33}) and O_{Q58} (black); O_{Y33} and N_{Q58} (red); (ii) O₂ and N_{Q58} (black); O₂ and O_{Y33} (red); (iii) O_{NO} and N_{Q58} (black); O_{NO} and O_{Y33} (red).

Tyr33 would also determine whether the N atom or the O atom of NO will react with O₂. In the present force field, based on ab initio calculations, the O_{NO} carries negative charge and hence is the H-bond acceptor. Consequently, it is the N_{NO} atom which reacts with O₂.

In summary, for the recombination of NO with oxy-trHbN, rate constants are of the order of several 10 ps over a wide range of Δ values. With decreasing Δ , the time constant for reaction I increases. It is found that the crossing geometry is little affected by varying Δ whereas the kinetics of the reaction depends somewhat on Δ . Analysis of the intermolecular interactions around the active site reveals that residues Tyr33 and Gln58 facilitate and guide the reaction to some extent.

Step II: NO₂ Dissociation. From six snapshots of trHbN–OONO, 10 ARMD trajectories of 50 ps each are started to study the homolytic cleavage of the peroxide bond with $\Delta = 50$ kcal/mol, which is close to the dissociation energy of O1–O2 bond ($\Delta_0 = 47.6$ kcal/mol). In none of these trajectories a reaction was observed. Analysis of the trajectories revealed that at the

equilibrium geometry of bound O₂NO, where the bond distance of the peroxide oxygens is about 1.4 Å, the dissociated state is energetically unfavorable due to large vdW repulsion between the two oxygen atoms of the peroxide bond. Figure 3A shows a one-dimensional potential energy curve of the bound and dissociated states along the O1–O2 bond distance. The bound state is a Morse potential associated with the O1–O2 bond, and the dissociated state is represented by the vdW and electrostatic interaction of O1 and O2 in the dissociated state. As the Figure suggests, the crossing of the two states with the present force field is at an O1–O2 distance of 2.25 Å and has an activation barrier of about 40 kcal/mol.

Blomberg et al. found a transition state for this step at an O1–O2 distance of 1.94 Å with an estimated barrier of 6.7 kcal/mol, which corresponds to simulation time scales of submicro- to microseconds, assuming an entirely diffusion-limited reaction to be occurring in the picoseconds time scale.^{56,57} To assess the sensitivity of this observation on the

Table 2. Brief Summary of ARMD Simulations of NO Dioxygenation in trHbN^a

Δ (kcal/mol)	no. of crossings (no. of trajectories)	duration of trajectories (ps)	total simulation time (ns)	time constant (ps) (coefficient)
trHbN–O₂ + NO → trHbN–OONO (Step I)				
60	60 (60)	50	3	1.3 (1.0)
30*	179 (180)	50	9	11 (1.0)
26	58 (60)	50	3	16 (1.0)
15	18 (60)	50	3	
5	0 (60)	50	3	
trHbN=O + NO₂ → trHbN–ONO₂ (Step III)				
68	60 (60)	50	3	3 (1.0)
59*	176 (180)	50	9	18 (1.0)
55	44 (60)	100	6	66 (1.0)
50	12 (60)	100	6	
40	0 (60)	100	6	
trHbN–ONO₂ → trHbN⁺ + NO₃[–] (Step IV)				
60*	173 (180)	100	18	30 (1.0)
50	37 (60)	100	6	80 (1.0)
30	3 (60)	100	6	
trHbN–OONO → trHbN–ONOO (Rearrangement)				
80*	171 (180)	100	18	10 (0.6), 46 (0.4)
75	41 (60)	100	6	80 (1.0)
70	12 (60)	100	6	
60	0 (60)	100	6	

^a The asterisks indicate the most probable Δ for a particular reaction.

parametrization, the vdW radius (σ_O) of the O1 and O2 atoms are varied between $1.0 \leq \sigma \leq 1.75$ Å on a grid with a separation of 0.05 Å. Five trajectories of 50 ps length were started from each of the six snapshots. For small values of σ , the reaction occurs rapidly since the vdW minimum is close to the equilibrium O1–O2 distance in the bound state. The O1–O2 distance at the crossing increases with increasing σ . Figure 3B shows the relationship between the O1–O2 distance at the crossings and σ_O . A geometry with an O1–O2 distance of 1.94 Å (DFT value) at the transition state corresponds to $\sigma_O = 1.55$ Å (see Figure 3B). Additional aspects of step II are addressed in the Discussion and Conclusions.

Step III: Rebinding of NO₂. In this step, the free NO₂ radical combines with the oxo-ferryl species (trHbN=O + NO₂) to give rise to a heme-bound nitrate complex. The reaction involves the formation of an O1–N bond which requires angular (O1–N–O2, O1–N–O, and Fe–O1–N), dihedral (Fe–O1–N–O2/O, N–O1–F–N(His)), and improper (N–O1–O2–O) terms to be included in the force field of the product state (Table 1). Following the discussion of step I, the dissociation energy of the O1–N Morse bond provides a first estimate of $\Delta_0 = 50.5$ kcal/mol for the asymptotic separation.

Six snapshots with dissociated NO₂ in trHbN were chosen to study reaction III for which multiple ARMD trajectories were run and the rebinding of NO₂ with trHbN-oxo species was followed with Δ between 40 and 68 kcal/mol. All results obtained are summarized in Table 2. For $\Delta = 68$ and 59 kcal/mol, most of the trajectories rebound, whereas for $\Delta = 55$ kcal/mol, 44 out of 60 trajectories showed crossing. On the other hand, for $\Delta = 50$ kcal/mol, 12 out of 60 trajectories showed crossing during 100 ps of simulation, while for $\Delta = 40$ kcal/mol, none of the 60 trajectories were found reactive.

The analysis reveals that the Fe–O1, O2–N, and O3–N distances during the crossing events are predominantly centered around their respective equilibrium values, whereas rebinding takes place over a broad range of O1–N distances (Figure S3

in the Supporting Information). The bound ONO₂ moiety remains planar during the crossing. Figure 4A shows that crossing occurs with a Fe–O1 distance varying between 1.6 and 1.7 Å. For $\Delta = 68, 59,$ and 55 kcal/mol, the crossings occur more toward the oxo-ferryl (reactant) side, whereas crossing geometries are rather more shifted toward the product side (heme–ONO₂) for $\Delta = 50$ kcal/mol (blue circles in Figure 4A). Figure 4A shows the two-dimensional view of the Fe–O1–N angle versus O1–N distance for $\Delta = 68, 59, 55,$ and 50 kcal/mol. For all values of Δ , the reaction occurs with a O1–N distance between 2.7 and 4 Å with a maximum around 3.2 Å, i.e., changing Δ by 20 kcal/mol leaves the crossing seam largely unaffected.

The time dependence of the crossing events is analyzed by calculating the survival probability of free NO₂ as a function of simulation time which was then fitted to an exponential function for $\Delta = 68, 59,$ and 55 kcal/mol. Table 2 reports the corresponding time constants and shows that the reaction is best described by a single exponential decay with τ in the range of a few tens of picoseconds. The time constants change by 1 order of magnitude for the different values of Δ : for $\Delta = 55$ kcal/mol $\tau = 66$ ps, which decreases to 18 and 3 ps for $\Delta = 59$ and 68 kcal/mol, respectively.

The H-bonding network between Tyr33, Gln58, and the ligands (Figure 4B) shows that for most of the crossing events the amide group of Gln58 and phenol group of Tyr33 are hydrogen bonded (Figure 4B). Here, TyrO acts as the H-bond acceptor of amide N. Similar to NO rebinding to heme–O₂, in the present case, Tyr33 remains close to the reacting ligands during the crossing (Figure 4B). In the majority of cases, Tyr33 is a H-bond donor to one of the O atoms of NO₂ (blue curve). Again, the H-bond between Tyr33 and NO₂ indicates the importance of Tyr33 residue, which arrests the movement of the ligand (NO₂), thus positioning it suitably for reaction III.

In summary, recombination of NO₂ to oxo-ferryl suggests a weak dependence of the crossing seam on Δ values. On the other hand, the rebinding dynamics is found to vary between 66 and 3 ps depending on the value of Δ , see Table 2. The fact that only 20% of the trajectories showed crossing for $\Delta_0 = 50$

(56) Nauser, T.; Koppenol, W. H. *J. Phys. Chem. A* **2002**, *106*, 4084–4086.

(57) van Holde, K. E. *Biophys. Chem.* **2002**, *101*, 249–254.

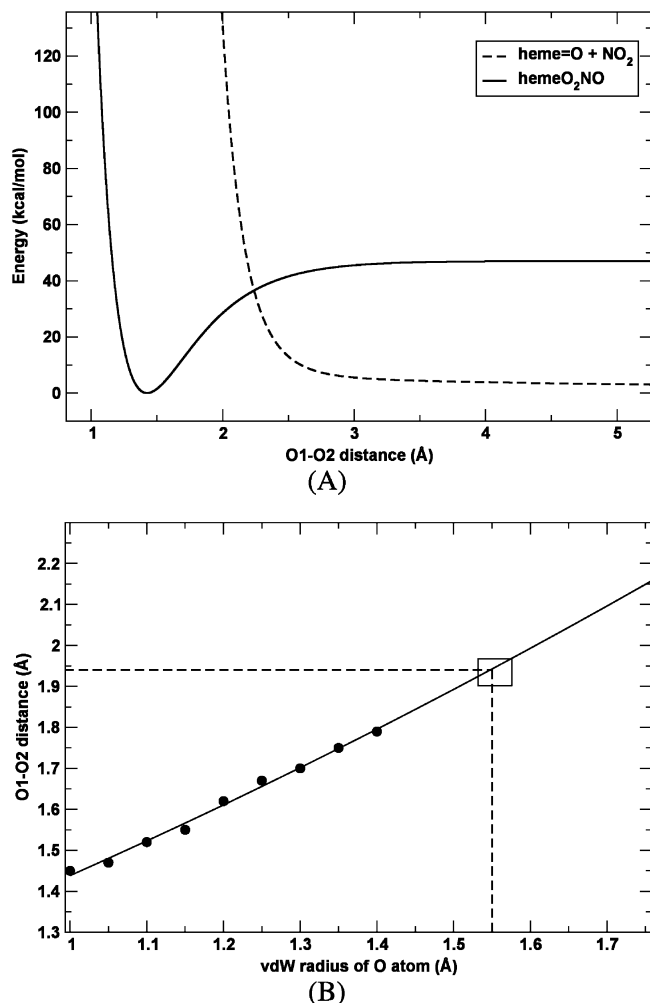


Figure 3. (A) One dimensional potential energy curve for heme-bound O₂NO (solid line) and NO₂ dissociated oxo-ferryl species (dashed line) along the O1–O2 distance. The bound state is given by the Morse potential of the O1–O2 bond in heme-bound O₂NO, and the dissociated state is given by the nonbonding interaction between the O atom of oxo-ferryl and the O atom of NO₂. (B) Average value of the O1–O2 distance during NO₂ dissociation against vdW radius of O atoms. A vdW radius of 1.55 Å is expected to provide NO₂ dissociation at 1.94 Å O1–O2 separation (the DFT value).

kcal/mol and no crossings were observed for $\Delta = 40$ kcal/mol suggest that $\tau \approx 100$ ps is rather a lower limit for this step. From the analysis of the interaction between the reactive ligands and active site amino acids Tyr33 and Gln58 appear to assist the reaction by interacting with the NO₂ radical and prepositioning it.

Step IV: Dissociation of NO₃⁻. Dissociation of nitrate involves breaking the Fe–O1 bond in the heme-bound nitrate complex. During step IV, the heme changes from hexa- to pentacoordinated. For this step, the dissociation energy of the Fe–O1 Morse bond provides a first estimate of $\Delta_0 = 50.7$ kcal/mol for the asymptotic separation. Therefore, we have studied the reaction for a range of Δ around this value.

From the six snapshots of trHbN–ONO₂, 10 ARMD trajectories of 100 ps each are started and dissociation of NO₃⁻ is followed with $\Delta = 60, 50,$ and 30 kcal/mol. Table 2 shows that with decreasing Δ , the number of crossing events decreases. For $\Delta = 30$ kcal/mol, only 3 of 60 trajectories dissociate within 100 ps while dissociation is more frequent for $\Delta = 50$ and 60 kcal/mol, see Table 2.

For $\Delta = 60$ and 50 kcal/mol, the distribution of crossing points along several coordinates is given in Figure S4 in the Supporting Information and Figure 5A shows two-dimensional plots of Fe–O1 distance against O1–N distance and Fe–O1–N angle together with the corresponding one-dimensional probability distributions. For both values of Δ , the reaction occurs with an Fe–O1 distance between 2 and 2.2 Å. Compared to the previous reaction steps, the dissociation of NO₃⁻ occurs in a relatively constrained geometric space. The fraction of undissociated NO₃⁻ as a function of simulation time is fitted to an exponential function, and the reaction is found monophasic with time constants varying between $\tau = 30$ ps for $\Delta = 60$ kcal/mol and $\tau = 80$ ps for $\Delta = 50$ kcal/mol (see Table 2). The H-bonding network between Tyr33, Gln58, and the nitrate ligand during the crossing events is shown in Figure 5B. During most of the crossing events, the amide group of Gln58 is H-bonded to the phenol group of Tyr33 (Figure 5B), where TyrO acts as a H-bond acceptor of amide N. During nitrate dissociation, both Tyr33 and Gln58 form H-bonds with the dissociating NO₃⁻, see Figure 5B.

In summary, reaction IV occurs over a wide phase space and the reaction seam does not strongly depend on Δ . The dynamics of the reaction are characterized by a single exponential decay with time constants on the order of a few tens of picoseconds. Similar to step III, the time constant $\tau = 80$ ps for $\Delta \approx \Delta_0$ suggests that the actual rate for this step is probably slower. The surrounding residues Tyr33 and Gln58 are found to participate in H-bonding with the dissociating ligand.

Tyr33Ala and Gln58Ala Mutation. For the four elementary steps investigated so far, residues Tyr33 and Gln58 are found to play more or less prominent roles as hydrogen-bond donors and acceptors. To further explore their role, we have studied each reaction step for three mutants: (i) Y33A, (ii) Q58A, and (iii) the double mutant Y33A/Q58A. For this, one of the starting structures was arbitrarily chosen and the three mutations were performed. The structures were optimized and equilibrated for 200 ps. For ARMD simulations, 40 trajectories were started from each of the three mutants for reactions steps I–IV with $\Delta = 30, 50, 59,$ and 60 kcal/mol, respectively, which are close to Δ_0 from the ab initio calculations. In addition, since the dependence of the crossing seam and the rate constants on the choice of Δ was found to be rather weak for all the reactions studied so far, the choice of Δ is not expected to greatly affect the results discussed in the following.

Step I. Recombination of NO with oxy-trHbN occurred in each of the 40 trajectories for all three mutants, and the observed crossing seam is wide as was the case for the wild-type protein. Figure 6 compares the crossing seam for the wild-type protein and its three mutants. The crossing occurs at a similar O2–N distance and O1–O2–N angle. Similar results are obtained for other internal coordinates (not shown). The fraction of unbound trajectories as a function of simulation time shows that for all mutants the rebinding is single exponential similar to the wild-type protein with similar time constants, see Table 3.

Step II. Similar to the wild-type protein, in none of the three mutants is NO₂ dissociation from peroxynitrite-trHbN observed.

Step III. For the wild-type protein with $\Delta = 59$ kcal/mol, 59 of the 60 trajectories showed NO₂ rebinding. On the other hand, for Y33A, Q58A, and Y33A + Q58A mutants, 10, 39, and 28 of the 40 trajectories, respectively, were reactive during 50 ps of simulations. The above results suggest that Q58A mutation has little effect on NO₂ rebinding. On the contrary, the Y33A mutation considerably reduces the number of crossing events.

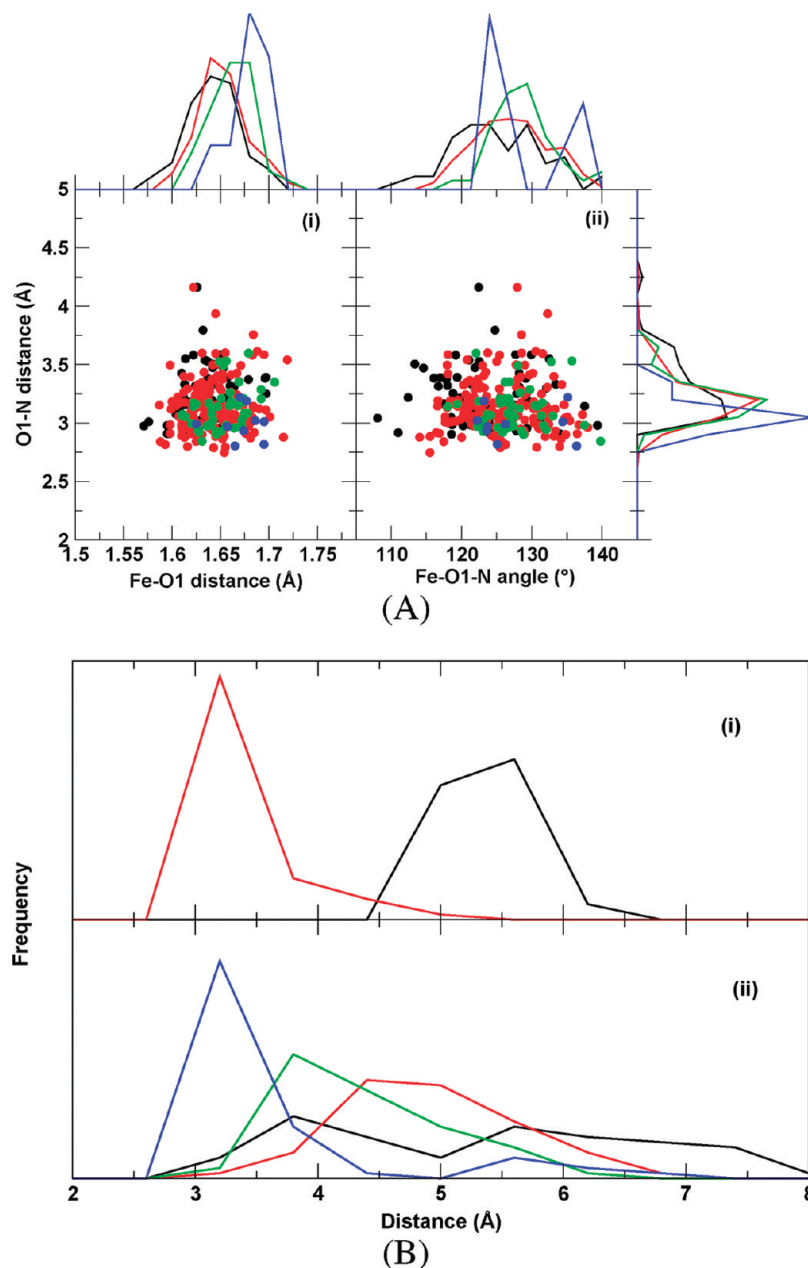


Figure 4. (A) Two-dimensional plot showing the correlated distribution of crossing points along (i) O1–N distance and Fe–O1 distance and (ii) Fe–O1–N angle and O1–N distance. The circles in black, red, green, and blue represent the crossings obtained for NO₂ rebinding with $\Delta = 68, 59, 55,$ and 50 kcal/mol, respectively. (B) Probability distribution of the H-bonding network between Q58, Y33, and NO₂ during the rebinding of NO₂. The distribution is shown for distances between (i) O atom of Y33 (O_{Y33}) and O_{Q58} (black); O_{Y33} and N_{Q58} (red); (ii) O1_{NO₂} and N_{Q58} (black); O1_{NO₂} and O_{Y33} (red); O2_{NO₂} and N_{Q58} (green); O2_{NO₂} and O_{Y33} (blue).

However, when both Y33 and Q58 are mutated to alanine, the number of crossing events increases compared to the Y33A mutant. The fraction of nonreactive trajectories as a function of simulation time are fitted to exponential functions. The time constants associated with the mutants are 201, 18, and 42 ps for Y33A, Q58A, and Y33A + Q58A, respectively. A detailed analysis of the crossing geometries shows that the NO₂ rebinding is largely controlled by Tyr33 and Gln58. The dynamic H-bonding network between the residues and the ligands is responsible for an efficient NO₂ rebinding in the wild-type protein. The large value of the time constant for Y33A mutant arises from the fact that only a small fraction of the trajectories exhibit crossings. Strictly speaking, the trajectories of 50 ps simulation time are inadequate to describe the dynamics

occurring at a time scale of 200 ps, despite the fact that we have run multiple trajectories with a cumulative simulation time of 2 ns.⁵⁸ However, for the present purpose, it suffices to say that the time constants associated with the Y33A mutant is significantly larger than that of the wild-type trHbN.

Step IV. During 50 ps of simulations, most of the trajectories in each of the three mutants exhibited nitrate dissociation. The crossing seam along the Fe–O1 distance and O1–N distance and Fe–O1 distance and Fe–O1–N angle are shown in Figure 7A for the three mutants as well as for the wild-type protein. The figure suggests a reduction of the Fe–O1 distance during crossing for the single mutants, i.e., Y33A and Q58A, whereas

(58) Fersht, A. R. *Proc. Natl. Acad. Sci. U.S.A.* **2002**, *99*, 14122–14125.

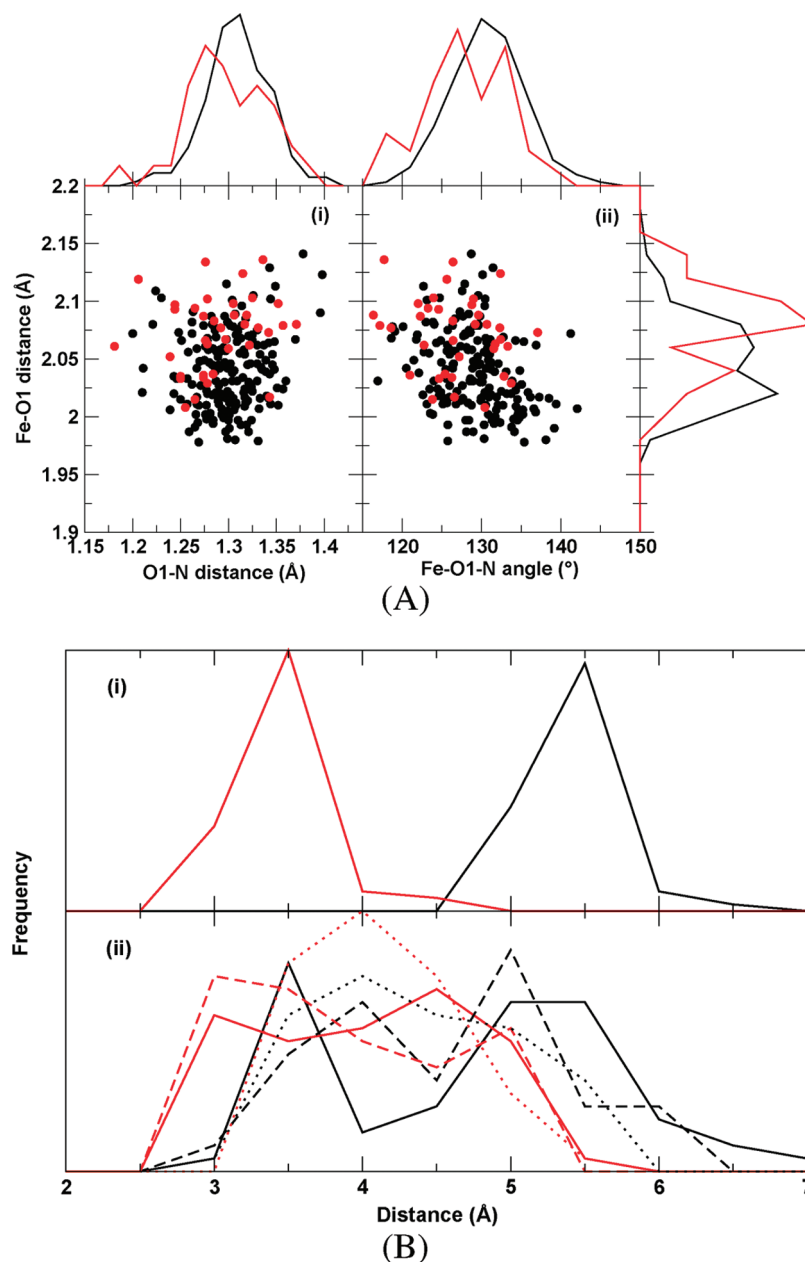


Figure 5. (A) Two-dimensional plot showing the correlated distribution of crossing points along the (i) O1–N distance and Fe–O1 distance and the (ii) Fe–O1–N angle and Fe–O1 distance. The circles in black and red represent the crossings obtained for NO₃⁻ dissociation with $\Delta = 60$ and 50 kcal/mol, respectively. (B) Probability distribution of the H-bonding network between Q58, Y33, and NO₂ during NO₃⁻ dissociation. The distribution is shown for distances between the (i) O atom of Y33 (O_{Y33}) and O_{Q58} (black); O_{Y33} and N_{O58} (red); (ii) O1, O2, and O3 atoms of NO₃⁻ and O_{Y33} (black); O1, O2, and O3 atoms of NO₃⁻ and O_{Y33} (red), shown in solid, dashed, and dotted lines, respectively.

for the double mutant it is indistinguishable from that of the wild-type protein. Figure 7B shows the kinetics of nitrate dissociation for the three mutants and the wild-type protein. While the wild-type protein and the double mutant show similar dissociation rates (with time constants about 30 ps), both single mutants show a faster nitrate dissociation compared to the wild-type protein. The kinetics of the single mutants are found to be best described by a double exponential function with time constants of 2 ps (coefficient 0.7) and 35 ps (coefficient 0.3) for the Y33A mutant and 8 ps (coefficient 0.9) and 35 ps (coefficient 0.1) for the Q58A mutant, see Figure 7B.

Similar to NO₂ rebinding (step III), the NO₃⁻ dissociation also shows a complicated protein dependence. While absence of one of the two H-bonding residues triggers a faster dissociation of the Fe–O1 bond at a shorter Fe–O1 distance, simul-

taneous mutation of the two bulky and H-bonding residues shows a similar crossing seam and kinetic pattern as that of the wild-type protein.

In summary, studies of the four reaction steps involved in NO dioxygenation have shown that (A) All steps but one (step II) can be investigated and analyzed in a meaningful way by ARMD. Step II is elusive and is also the one that has not been found in experiments.^{12,16} (B) Investigations of single and double mutants establish that for specific elementary steps (steps III and IV in particular) the protein plays an active role through H-bond formation to the reacting species. The fact that step II could not be followed and no direct experimental evidence for formation of NO₂ is available prompts us to study an alternative pathway.

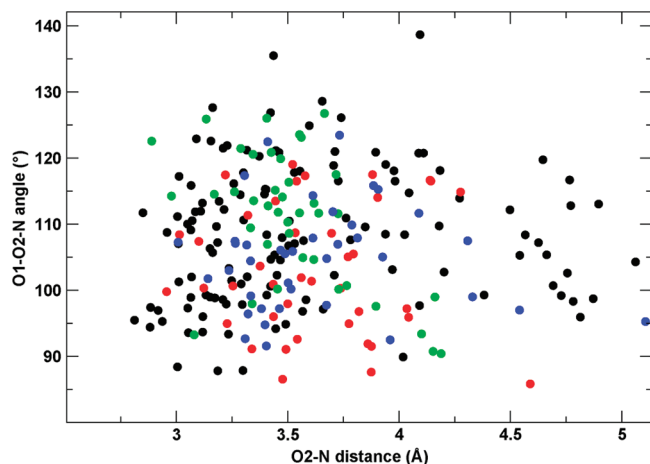


Figure 6. Two-dimensional plot showing the correlated distribution of crossing points, during the NO recombination reaction, along the O2–N distance and O1–O2–N angle for the wild-type protein (black), Y33A (red), Q58A (green), and Y33A + Q58A (blue) mutants with $\Delta = 30$ kcal/mol.

Table 3. Summary of Time Constants (in Picoseconds) for the wt-trHbN and Its Three Mutants during NO Dioxygenation

	step I $\Delta = 30$ kcal/mol	step III $\Delta = 59$ kcal/mol	step IV $\Delta = 60$ kcal/mol	rearrangement $\Delta = 80$ kcal/mol
wt-trHbN	11	18	30 (1.0)	10 (0.6), 46 (0.4)
Y33A	4	201	2 (0.7), 35 (0.3)	193
Q58A	6	18	8 (0.9), 35 (0.1)	20
Y33A + Q58A	6	42	27	262

Alternative Pathway. Previously, the barrier associated with step II has been estimated to be 6.7 kcal/mol by Blomberg et al.¹⁸ Such a large barrier suggests that the reaction occurs on a submicro- to microsecond time scale, which is too slow to be observed in the present simulations. Furthermore, with an overall rate of NO dioxygenation of $7.5 \times 10^8 \text{ M}^{-1} \text{ s}^{-1}$, it raises doubts if the reaction indeed occurs via this step. Under normal physiological conditions, Herold et al. were unable to observe any dissociated NO_2 .^{12,16} The lack of experimental detection of free NO_2 during NO dioxygenation has led to the suggestion of an alternative mechanism. It was postulated that, after NO rebinding with oxy-Hb, the peroxynitrite ($-\text{OONO}$) complex undergoes a rearrangement to a nitrate ($-\text{ONO}_2$) complex.^{12,59} The rearrangement of peroxynitrite to nitrate catalyzed by metallo-porphyrins are well-known for 5,10,15,20-tetrakis(*N*-methyl-4'-pyridyl) porphinatoiron(III) [FeIII(TMPyP)] or 5,10,15,20-tetrakis(2,4,6-trimethyl-3,5-sulfonatophenyl) porphinatoiron(III) [FeIII(TMPS)]^{60,61} and for mutated myoglobin (H64A and H64D),⁶² where it was shown that the reactivity of metMb(III) toward peroxynitrite depends on the presence of the distal histidine (H64).

The peroxynitrite to nitrate rearrangement reaction involves breaking of the O1–O2 and O2–N bonds in trHbN–OONO

and simultaneous formation of an O1–N bond in trHbN–ONO₂, see the inset in Figure 8B. Rearrangement then leads to a large change in the O1–O2–N angle of the peroxynitrite complex and O1–N–O2 angle of the nitrate complex. To study such a process, we used a topology in which OONO and the nitrate (ONO₂) ligands are described by bonds instead of bonds, angles, and dihedrals. For example, the force field for OONO is given by

$$V_{\text{OONO}} = V_{\text{O1-O2}} + V_{\text{O2-N}} + V_{\text{O1-N}} + V_{\text{O1-O}} + V_{\text{O2-O}} + V_{\text{N-O}} \quad (3)$$

where, except for the last term on the right-hand side (the N–O bond), all other bonds are described by the Morse potentials. Since the N–O bond undergoes little change in conformation from reactant to product, a harmonic potential is sufficient.

To study trHbN–OONO to trHbN–ONO₂ rearrangement, we considered six snapshots of heme-bound peroxynitrite and carried out several ARMD trajectories for a range of Δ values. The initial estimate of Δ_0 for this reaction is obtained from the sum of the dissociation energies of O1–O2 and O2–N Morse potentials, which amounts to 72 kcal/mol. Therefore, we have carried out simulations with $\Delta = 60, 70, 75,$ and 80 kcal/mol, see Table 2. For $\Delta = 80$ kcal/mol, 171 of 180 trajectories crossed while for $\Delta = 75$ and 70 kcal/mol, 41 and 12 of 60 trajectories reacted. For $\Delta = 60$ kcal/mol, none of the trajectories are found reactive on the time scale of the simulations (100 ps).

A time series of the energy associated with the rearrangement of the peroxynitrite to the nitrate complex for both the reactant and the product states is shown in Figure 8A. In this trajectory, crossing occurs after 38 ps and the energy of the product state after crossing is lower by about 25 kcal/mol compared to the energy of the reactant before crossing. Figure 8A also shows the time evolution of the O1–O2 and O1–N bonds and the O1–N–O2 and O1–O2–N angles where rearrangement is accompanied by substantial changes of the bonds and angles involved in the reaction. During the crossing, the O1–O2 bond of trHbN–OONO breaks and the O1–N bond of trHbN–ONO₂ is formed. The breaking and formation of these bonds also lead to changes in the corresponding valence angles, see Figure 8A.

The distribution of Fe–O1, O1–O2, O2–N, O–N, O1–N distances as well as for O1–O2–N and O1–N–O2 angles along the crossing seam for $\Delta = 80, 75,$ and 70 kcal/mol are shown in Figure S5 in the Supporting Information. The analysis reveals that crossings occur over a range of O1–N distances between 2.3 and 2.7 Å, with a peak at 2.47 Å, which is close to the equilibrium O1–N distance in the reactant. Figure 8C shows two-dimensional plots of the crossing seam along (i) O1–N and O1–O2 and (ii) O1–N and O1–O2–N coordinates for $\Delta = 80, 75,$ and 70 kcal/mol together with the corresponding one-dimensional distributions. The crossing seam is broad in these coordinates. A smaller value of Δ results in crossings with a comparatively longer O1–O2 distance, see the probability distribution along O1–O2 coordinate for $\Delta = 70$ kcal/mol. Similar to other reaction steps, the crossing seam moderately depends on Δ .

The fraction of trajectories without rearrangement as a function of simulation time $p(t)$ is analyzed for $\Delta = 80$ and 75 kcal/mol. $p(t)$ for $\Delta = 80$ kcal/mol can be fit to a double exponential with two time constants: $\tau_1 = 10$ ps and $\tau_2 = 46$ ps with coefficients 0.6 and 0.4, respectively. On the other hand, for $\Delta = 75$ kcal/mol, the underlying kinetics can be described

(59) Gardner, P. R. *J. Inorg. Biochem.* **2005**, *99*, 247–266.

(60) Stern, M. K.; Jensen, M. P.; Kramer, K. *J. Am. Chem. Soc.* **1996**, *118*, 8735–8736.

(61) Lee, J.; Hunt, J. A.; Groves, J. T. *J. Am. Chem. Soc.* **1998**, *120*, 7493–7501.

(62) Herold, S.; Matsui, T.; Watanabe, Y. *J. Am. Chem. Soc.* **2001**, *123*, 4085–4086.

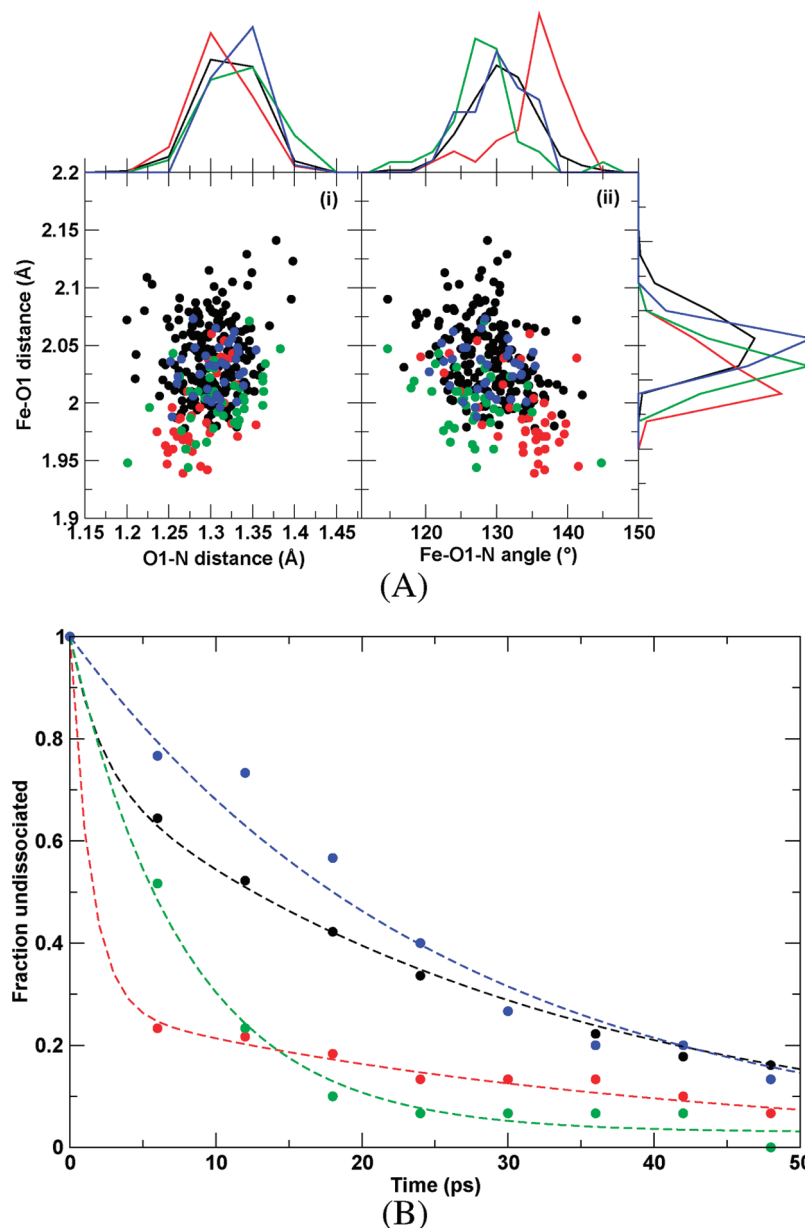


Figure 7. (A) Two-dimensional plot showing the correlated distribution of crossing points along the (i) O1–N distance and Fe–O1 distance and the (ii) Fe–O1–N angle and O1–N distance during the nitrate dissociation reaction for $\Delta = 60$ kcal/mol. The circles in black, red, green, and blue represent the crossings obtained for the wild-type protein (black), Y33A (red), Q58A (green), and Y33A + Q58A (blue) mutants. (B) Time distribution of the fraction of trajectories without nitrate dissociation in the case of the wild-type protein (black), Y33A (red), Q58A (green), and the Y33A + Q58A (blue) mutants for $\Delta = 60$ kcal/mol.

with a single exponential with time constant 80 ps. These results suggest that Δ has a substantial effect on the kinetics of the reaction, and with decreasing Δ , the reaction slows down. However, for a detailed understanding of the slow processes, longer simulations are required.

To study the role of protein in the rearrangement of peroxynitrite to nitrate complex, we started 40 trajectories of 100 ps duration each, with $\Delta = 80$ kcal/mol, from each of the three mutants studied in this work. Out of 40 trajectories, 19, 39, and 16 trajectories showed rearrangement for Y33A, Q58A, and Y33A/Q58A mutants, respectively. The fraction of trajectories without reaction is plotted against simulation time for the wild-type trHbN along with its three mutants, see Figure 8D. The time constants associated with the rearrangement reaction are determined as 193, 20, and 262 ps for Y33A, Q58A, and Y33A/Q58A mutants, respectively (see Table 3).

In summary, the rearrangement of peroxynitrite complex of trHbN to its nitrate complex is studied with four values of Δ between $\Delta = 60$ and 80 kcal/mol. For $\Delta = 80$ kcal/mol, the rearrangement reaction shows biphasic kinetics with time constants of 10 and 46 ps. Whereas for $\Delta = 75$ kcal/mol, a single exponential function with a time constant of 80 ps is found to explain the underlying kinetics. With comparison of the results of wild-type trHbN and three mutants, it is found that the rearrangement reaction is strongly influenced by the mutation of Tyr33 residue whereas Gln58 residue is found to have rather small effects on the reaction, see Table 3.

Discussion and Conclusions

Nitric oxide plays a pivotal role in various physiological processes. It is now widely believed that oxy-bound globins can oxidize toxic NO to harmless nitrate. Here we have used

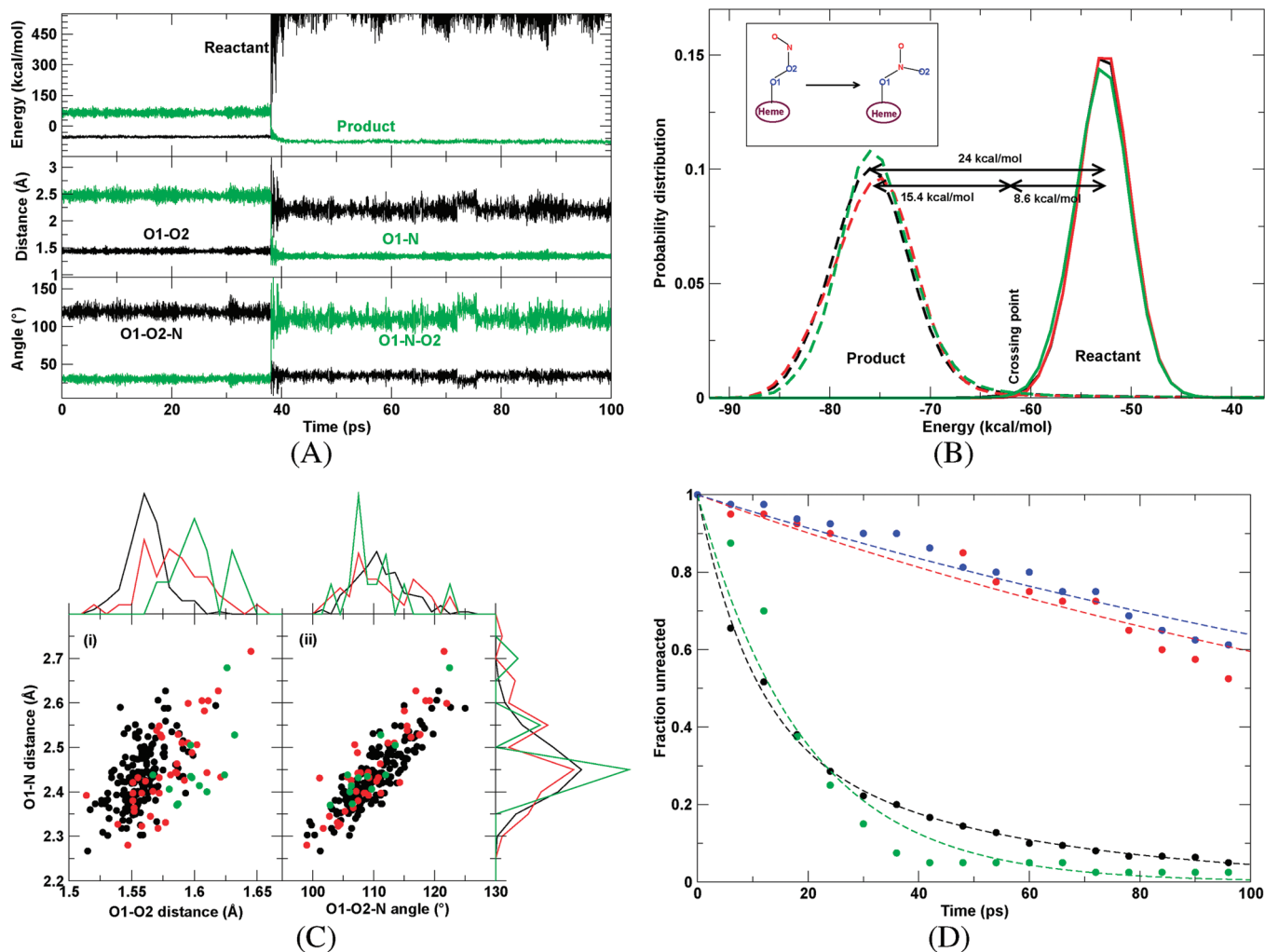


Figure 8. (A) Time series of the energy of the reactant and product, the O1–O2 and O1–N bond distances, and the O1–O2–N and O1–N–O2 angles during an example ARMD trajectory for OONO rearrangement reaction. In this trajectory, reaction occurs after 38 ps of simulation with $\Delta = 80$ kcal/mol. (B) Probability distribution of the energy of the reactant (solid line) and the product (dashed line) obtained from 300 independent ARMD trajectories. The distributions $p(E)$ shown by black, red, and green lines correspond to $\Delta = 80, 75,$ and 60 kcal/mol, respectively. The region where the reactant and product distributions overlap represents the crossing region. (C) Two-dimensional plot showing the correlated distribution of crossing points along the (i) O1–N distance and O1–O2 distance and the (ii) O1–O2–N angle and O1–O2 distance for $\Delta = 80$ (black), 75 (red), and 70 (green) kcal/mol. (D) Time distribution of fraction of unreacted trajectories for wt-trHbN (black), Y33A (red), Q58A (green), and Y33A + Q58A (blue) mutants for $\Delta = 80$ kcal/mol.

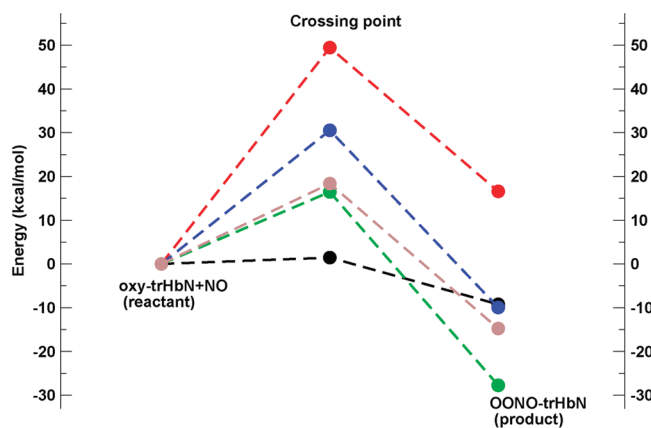


Figure 9. Relative potential energies determined from DFT calculation of snapshots corresponding to the reactant, product, and the crossing points obtained from five ARMD trajectories for the reaction step I.

atomistic and molecular dynamics simulations to characterize the NO dioxygenation in truncated hemoglobin of *Mycobacterium tuberculosis* by considering two pathways, A and B.

Pathway A follows earlier suggestions^{14,15,18,38} where the entire reaction consists of four steps: (I) NO (re)binding to oxy-trHbN, (II) homolytic cleavage of the peroxide bond in trHbN–OONO, (III) NO₂ rebinding to oxo-ferryl trHbN, and (IV) dissociation of nitrate from trHbN–ONO₂ complex, whereas pathway B involves a rearrangement reaction from peroxytrinitrite–trHbN to the trHbN–ONO₂ complex.^{12,59} The reactive steps were followed by employing the adiabatic reactive MD method which was found earlier to provide a detailed atomistic understanding of NO rebinding in myoglobin.^{42,43} For the reactant and product state of each step, associated force-fields were determined from electronic structure calculations. For pathway A, steps I, III, and IV yield rate constants on the picosecond time scale. To assess the sensitivity of the results, the simulations for each of the reaction steps are run for a range of Δ values around the ab initio determined value. The results obtained from these simulations are found to be robust and show little dependence on the precise value of Δ . However, it is possible that more elaborate treatments of Δ , such as including an explicit conformational dependence, provides additional insight.

To further characterize step II (not reactive so far), 30 additional trajectories 200 ps in length with an oxygen-van der Waals radius of $\sigma_{\text{O}} = 1.55 \text{ \AA}$ were analyzed. None of them were reactive. Thus, for typical and realistic values of σ_{O} , the rate for homolytic cleavage is slower than nanoseconds. To quantify the activation energy associated with NO_2 dissociation, the free-energy profile along the O1–O2 distance was calculated from three independent umbrella sampling simulations at 300 K and analyzed with the weighted histogram analysis method.^{63,64} The resulting free energy profiles (Figure S6 in the Supporting Information) exhibit NO_2 dissociation barriers of 12–15 kcal/mol, which are in qualitative agreement with an estimated barrier of 6.7 kcal/mol from previous DFT calculations.¹⁸ On the other hand, for pathway B, the rearrangement reaction, rate constants were found to be in the picosecond range, which readily explains the rapid overall NO dioxygenation that is associated with a second order rate constant of $7.5 \times 10^8 \text{ M}^{-1} \text{ s}^{-1}$ in trHbN.²⁹ Moreover, Herold et al. were unable to observe any dissociated NO_2 which should emerge along pathway A. All these observations suggest that pathway B may be preferred.^{12,16} It is also of interest to put such rates into context with caged radical reactions, which are characteristic of cytochrome P450 catalyzed oxidations. Employing *trans*-2-phenyl-methylcyclopropane as a radical clock-substrate of a P450 enzyme mimic, i.e., a synthetic Fe(IV)=O porphyrin radical cation, a lifetime of 625 fs for the radical intermediate was estimated.⁶⁵

A detailed analysis of the energetics of pathway B is shown in Figure 8B, which reports the probability distribution $p^{\text{R}}(E)$ of the energy of the reactant (peroxynitrite complex) and that of the product (nitrate complex) $p^{\text{P}}(E)$ as sampled by reactive MD simulations (average over 300 independent trajectories, each 100 ps in length). As can be seen, the product state is stabilized by 24 kcal/mol, which is in reasonable agreement with the relative stabilization energy obtained from quantum chemical calculations of the model heme systems from both, the present work (37.1 kcal/mol), and by Blomberg et al.¹⁸ (35.6 kcal/mol). The distributions $p^{\text{R}}(E)$ (solid line) and $p^{\text{P}}(E)$ (dashed line) overlap at 8.6 kcal/mol above the most probable energy of the reactant, see Figure 8B. This low probability region corresponds to the crossing from reactant to product and is only a little influenced by the choice of Δ . To more quantitatively characterize the forward and reverse barriers, the transition state structure was optimized by quantum chemical calculations of the model system using the quadratic synchronous transit method.^{66,67} The calculated TS barrier is 8.3 kcal/mol, which supports the results from the simulations. However, the quantum chemical calculations do not include entropy corrections and interactions with the protein and solvent environment whereas ARMD includes such effects. The TS structure obtained from quantum chemical calculations (Supporting Information) has striking similarities with the crossing geometries obtained from the ARMD simulations of the rearrangement reaction, which further validates the parametrization of the force fields.

It is also of interest to more carefully compare the structure and spectroscopic properties of the NO_2 fragment in the TS structure and free NO_2 from B3YLP/6-31G(d,p) calculations.

While free NO_2 has two symmetric N–O bonds (1.26 Å) and an ONO angle of 101° , NO_2 at the TS is asymmetric with NO bond distances of 1.26 and 1.21 Å and an ONO angle of 124° . Additionally, the bending and stretching frequencies of NO_2 in the two structures differ considerably (764, 766, 1486 cm^{-1} for free NO_2 and 797, 1180, 1552 cm^{-1} for NO_2 at the TS; a frequency analysis of the entire model complex at the TS yields vibrations with strong involvement of the NO_2 at 739, 748, 1088, and 1609 cm^{-1}). Thus, NO_2 at the TS of the NO dioxygenation has properties quite different from that of “free” NO_2 as has been pointed out previously.¹⁸

Comparing the two pathways studied in this work, there is strong evidence that pathway B is favorable and realistic both in view of the energetics and the geometrical properties which compare favorably with electronic structure calculations. However, given that observing the dissociation of NO_2 (step II) in pathway A depends on the van der Waals parameters used (see above), more detailed analysis of this step may be required to rule out pathway A. Finally, the barriers for individual crossing events can be controlled through the force field parametrizations for the product and the reactant states.

It is known that the rate of NO dioxygenation varies substantially in different heme proteins,^{32,68,69} suggesting that the particular environment around the active site is important. Here, the role of the protein environment is assessed through simulations of alanine mutants Y33A and Q58A and their combination. From previous experimental and computational studies it is known that Tyr33 and Gln58 residues participate in a dynamic H-bonding network with the heme-bound and free ligands.^{33,70–72} A previous QM/MM study of the reactive steps along pathway A suggested that Y33 does not play a significant role in the reaction,³⁸ although experimental studies using the Y33F mutant observe an increase in NO_2 dissociation and a decrease in NO dioxygenation rates compared to wild-type trHbN.²⁹ Similar results are also obtained in *Escherichia coli* flavohemoglobin where the rate of NO dioxygenation decreases by ≈ 30 -fold upon Y33F mutation.⁷³ Finally, in Hbs of parasitic worm *Ascaris lumbricoides* (also known as *Ascaris* Hb or AHb), the strategic positioning of a Cys residue in the distal side⁷⁴ enables the organism to carry out the cysteine-mediated dioxygenase reaction in the presence of NO via an S-nitrosothiol intermediate.⁷⁵ This illustrates the diversity of interaction of NO with Hb of different organisms, which has been discussed in more detail in a recent review.³⁰

A detailed picture of the role of active site residues on the NO dioxygenation in trHbN emerges from the present simulations. They show that step I is minimally influenced by the protein environment, which is in agreement with previous observations where NO is found to be extremely reactive toward oxygenated globins because the bound oxygen has a dominant superoxide character.^{11,56} Similar to the wild-type protein,

- (63) Kumar, S.; Rosenberg, J. M.; Bouzida, D.; Swendsen, R. H.; Kollman, P. A. *J. Comput. Chem.* **1995**, *16*, 1339–1350.
(64) Roux, B. *Comput. Phys. Chem.* **1995**, *91*, 275–282.
(65) Sbaragli, L.; Woggon, W. D. *Synthesis* **2005**, 1538–1542.
(66) Halgren, T. A.; Lipscomb, W. N. *Chem. Phys. Lett.* **1977**, *49*, 225–232.
(67) Peng, C.; Ayala, P. Y.; Schlegel, H. B.; Frisch, J. J. *J. Comput. Chem.* **1996**, *17*, 49.

- (68) Ascenzi, P.; Bolognesi, M.; Milani, M.; Guertin, M.; Visca, P. *Gene* **2007**, *398*, 42–51.
(69) Ascenzi, P.; Visca, P. *Methods Enzymol.* **2008**, *436*, 317–337.
(70) Yeh, S.-R.; Couture, M.; Ouellet, Y.; Guertin, M.; Rousseau, D. L. *J. Biol. Chem.* **2000**, *275*, 1679–1684.
(71) Ouellet, Y.; Milani, M.; Couture, M.; Bolognesi, M.; Guertin, M. *Biochemistry* **2006**, *45*, 8770–8781.
(72) Mishra, S.; Meuwly, M. *Biophys. J.* **2009**, *96*, 2105–2118.
(73) Gardner, A. M.; Martin, L. A.; Gardner, P. R.; Dou, Y.; Olson, J. S. *J. Biol. Chem.* **2000**, *275*, 12581–12589.
(74) Yang, J.; Kloek, A. P.; Goldberg, D. E.; Mathews, F. S. *Proc. Natl. Acad. Sci. U.S.A.* **1995**, *92*, 4224–4228.
(75) Minning, D. M.; Gow, A. J.; Bonaventura, J.; Braun, R.; Dewhirst, M.; Goldberg, D. E.; Stamler, J. S. *Nature* **1999**, *401*, 497–502.

reaction II did not occur in the mutants. Unlike reaction I, our simulations reveal that NO₂ rebinding (step III) is strongly influenced by Tyr33 and Gln58. For the Y33A mutant, the time constant differs by an order of magnitude from that of wild-type trHbN (see Table 3). This can be explained by noting that in wild-type trHbN the oxygen atom of the oxo-ferryl species is stabilized via H-bonding to Gln58, and the free NO₂ radical participates in H-bonding with both Tyr33 and Gln58 which arrest the free ligand and make it available for reaction. Thus step III is not entirely diffusion controlled. Instead, the reaction in the wild-type protein is facilitated by the presence of Tyr33 and Gln58. Nitrate dissociation (step IV) as well as the rearrangement of trHbN–OONO to trHbN–ONOO are also found to be influenced by residues Tyr33 and Gln58. In general, Tyr33 and Gln58 facilitate the reaction by preorienting the ligands via H-bonding, which is not possible for the corresponding alanine mutants. This is contrary to previous findings which reported that the protein environment plays no role in the NO dioxygenation reaction.³⁸ Our simulations reflect the importance of Tyr33, which is conserved across the trHb family, suggesting an evolutionary significance of the residue.⁷⁶ One possible origin for the different conclusions concerning the role of the protein environment is that the QM/MM calculations involved restrained energy minimizations along a predefined progression coordinate instead of a fully flexible and sufficiently long explicit dynamics simulations, which is not possible with QM/MM for large systems.³⁸

Until now, no generally accepted scheme for the elementary steps involved in NO dioxygenation is available. The nature of the intermediate is expected to be different for different globins and will also depend on the experimental conditions such as concentration of NO and O₂ and pH, as well as the existence, proximity, and nature of the reductase domain.^{8,30} In other words, given the differences between Hbs of different organisms on one side and differences between various globins on the other,³⁰ mechanistic insight from the reaction investigated here (conversion of NO to nitrate in trHbN) cannot straightforwardly be generalized to NO dioxygenation in other proteins. Extensive experimental work over the past few years has led to the conclusion that under physiological conditions flavohemoglobin binds NO at the heme, reduces it to nitroxyl, and reacts with O₂ to form nitrate,⁸ although the intermediates of this pathway have as yet not been studied. In FHbs, the ferric heme is reduced to the ferrous form by methemoglobin reductases together with NADH and the FAD prosthetic group, thus completing the catalytic cycle.²⁴ The kinetics for NO dioxygenation in oxy-trHbN is studied in vitro under aerobic conditions,²⁹ although in vivo trHbN operates at microaerobic conditions. Thus, the relevance of single step turnover studies starting from O₂-bound heme to the in vivo situation should be seen in this context. Nonetheless, the in vitro NO dioxygenation of trHbN, which possesses high O₂ affinity ($P_{50} = 0.013$), suggests that trHbN protects aerobic respiration from NO inhibition.²⁹

(76) Nardini, M.; Pesce, A.; Milani, M.; Bolognesi, M. *Gene* **2007**, *398*, 2–11.

In the present work, we have investigated the mechanistic details of NO dioxygenation in oxy-trHbN by studying two pathways. While proposed pathway A occurs via peroxide bond cleavage, pathway B involves a rearrangement of heme–OONO to heme–ONO₂. Experimentally determined second order rate constants for NO dioxygenation are of the order of $10^8 \text{ M}^{-1} \text{ s}^{-1}$ for oxy-trHbN. Since the diffusion controlled migration of NO to the heme-active site is generally believed to be the slowest process, it is conceivable that the elementary reactive steps at the active site should be fast, i.e., on the order of pico- to nanoseconds. This is also the case in Mbs, where the rebinding times for NO and CO are between several tens of picoseconds and hundreds of nanoseconds.^{77–84} In the present simulations, which explicitly include nuclear dynamics, solvation, and protein environmental effects, all elementary steps were found to be in this time range, except for step II. For this step, the product (NO₂) could not be characterized experimentally and electronic structure calculations give a high barrier leading to microsecond time scales, which is probably too slow to be compatible with the measured rate constants. Thus, pathway B, the rearrangement of the Fe(III)OONO intermediate to nitrate, appears to be favorable for NO dioxygenation in trHbN. Future experiments using time-resolved methods both in vivo as well as in vitro should be able to discriminate between pathways A and B, which will lead to fundamental understanding of the NO dioxygenation reaction. It will also be of considerable interest to study NO dioxygenation in different proteins, including Mb and Hb, to obtain insights into similarities and differences in the mechanistic aspects of the reaction.

Acknowledgment. The authors thank Stephan Lutz for many helpful discussions, Profs. P. E. M. Siegbahn and K. M. Merz for stimulating comments and useful suggestions from an anonymous reviewer. Generous allocation of computing time at the Centro Svizzero di Calcolo Scientifico (CSCS) is gratefully acknowledged. This work has been supported through Grant 200021-117810 by the Swiss National Science Foundation.

Supporting Information Available: A brief discussion on the force field parameters obtained from ab initio calculations, optimized geometries of the reactive intermediates in Cartesian coordinates, some additional tables and figures, and complete citation for refs 44, 52, and 79. This material is available free of charge via the Internet at <http://pubs.acs.org>.

JA9078144

- (77) Austin, R. H.; Beeson, K. W.; Eisenstein, L.; Frauenfelder, H.; Gunsalus, I. C. *Biochemistry* **1975**, *14*, 5355–5373.
(78) Petrich, J. W.; Lambry, J. C.; Kuczera, K.; Karplus, M.; Poyart, C.; Martin, J. L. *Biochemistry* **1991**, *30*, 3975–3987.
(79) Steinbach, P. J.; et al. *Biochemistry* **1991**, *30*, 3988–4001.
(80) Ansari, A.; Jones, C. M.; Henry, E. R.; Hofrichter, J.; Eaton, W. A. *Biochemistry* **1994**, *33*, 5128–5145.
(81) Kim, S.; Jin, G.; Lim, M. *J. Phys. Chem. B* **2004**, *108*, 20366–20375.
(82) Banushkina, P.; Meuwly, M. *J. Phys. Chem. B* **2005**, *109*, 16911–16917.
(83) Danielsson, J.; Banushkina, P.; Nutt, D. R.; Meuwly, M. *Int. Rev. Phys. Chem.* **2006**, *25*, 407.
(84) Banushkina, P.; Meuwly, M. *J. Chem. Phys.* **2007**, *127*, 13501.